PAPER

Check for updates

Encouraging tribomechanical and biological responses of hydroxyapatite coatings reinforced by various levels of niobium pentoxide particles†

Mir Saman Safavi,*[ab] Jafar Khalil-Allafi, [iD] *[a] Amir Motallebzadeh,[c] Cristina Volpini, [iD] [b] Vida Khalili[d] and Livia Visai [iD] *[be]

The development of surface technologies to obtain improved tribomechanical and biological characteristics of synthetic NiTi implants is critical. A suitable match with the mechanical properties of the implanted biomaterial is necessary to reduce the risk of stress-shielding and implantation failure. The present contribution has attempted to assess the influence of the Nb_2O_5 particle level in an electrolyte, *i.e.*, 0–1 g L^{-1}, on the tribomechanical and biological performance of the HAp layers, which were obtained by galvanostatic pulse electrodeposition on NiTi. The surface characteristics of the electrode-posited layers were analyzed using GIXRD, FESEM, XPS, and contact angle measurements. Nanoindentation, nanoscratch, and pull-off assays were employed to study the tribomechanical properties of the films. The *in vitro* biocompatibility of the developed specimens was investigated using NIH3T3 fibroblast cells. The results illustrated that a more compact and hydrophilic surface is obtained with the incorporated particles. The Nb content and Ca/P molar ratio are increased from the outermost surface to the subsurface layers of the coatings. The composite coatings showed higher hardness, elastic modulus, bonding strength to the underlying NiTi, and lower COF compared to pure HAp layers. The elastic modulus of the Nb_2O_5-reinforced HAp films is close to that of cortical bone, reducing stress-shielding risk. The inclusion of Nb_2O_5 particles in the HAp matrix led to an improvement in cell functions, *e.g.*, viability and proliferation, within the various cell culture durations. The adopted surface modification strategy in this work can create new opportunities for the successful use of NiTi in orthopedic applications.

1. Introduction

The surface properties of a material, as an interface between the material and the environment, decide its performance and service lifetime. Simply, the initial interactions between a material and the surrounding environment occur at its surface.

It is important to adopt desirable surface modification approaches not only to tackle the challenges facing bulk materials but also to further increase their beneficial properties. Therefore, it is possible to tailor the surface properties of a material to simultaneously exploit the beneficial properties of bulk and the surface for a specific application.[1–4] There are a variety of surface technologies, including electrochemical deposition, plasma spraying, magnetron sputtering, chemical vapor deposition, physical vapor deposition, and laser deposition, that have been developed to meet the requirements of various industrial fields. The coatings produced by vacuum-based and spraying technologies show high adhesion strength to the substrate; however, the electrodeposition engaged a specific position in the surface finishing industry of the synthetic biomaterials thanks to its simplicity and cost-effectiveness. The technique allows fabricating uniform layers and incorporating one or more reinforcing agents into the growing film.[5–9]

NiTi shape memory alloys, falling under the category of metallic biomaterials, exhibit noticeable superelasticity, high

[a] *Research Center for Advanced Materials, Faculty of Materials Engineering, Sahand University of Technology, P.O. Box: 51335-1996, Tabriz, Iran. E-mail: samansafavi1992@gmail.com, jallafi@yahoo.de; Fax: +98 4133449454; Tel: +98 4133449454*

[b] *Molecular Medicine Department (DMM), Center for Health Technologies (CHT), UdR INSTM, University of Pavia, Via Taramelli 3/B, 27100 Pavia, Italy. E-mail: livia.visai@unipv.it*

[c] *Koç University Surface Science and Technology Center (KUYTAM), Koç University, İstanbul, Turkey*

[d] *Institut für Werkstoffe, Ruhr-Universität Bochum, Universitätsstrasse 150, D-44780 Bochum, Germany*

[e] *Medicina Clinica-Specialistica, UOR5 Laboratorio di Nanotecnologie, ICS Maugeri, IRCCS, 27100 Pavia, Italy*

† Electronic supplementary information (ESI) available. See DOI: https://doi.org/10.1039/d3ma00704a

corrosion resistance, suitable biocompatibility, and moderate elastic modulus (28–40 and 70 GPa in martensite and austenite phases, respectively). Thanks to its encouraging properties, NiTi is commonly used in various clinical branches, such as orthopedics, cardiovascular, and orthodontics.[10–12] One potential challenge that threatens the success of orthopedic surgeries is the mismatch between the elastic modulus of the implanted material and the natural bone, which can cause a the stress-shielding phenomenon. The stress-shielding refers to the decrease in bone density due to the reduced/removed stress on the bone, as the synthetic implant with a higher elastic modulus takes the applied load. It may also lead to poor bone growth and cell death.[13,14] NiTi has the lowest elastic modulus among the commercially available metallic biomaterials; however, it is necessary to minimize the mismatch between the elastic modulus values of the cortical bone (15–30 GPa) and NiTi (28–40 and 70 GPa in martensite and austenite phases, respectively). Moreover, an increase in the hardness of the implanted material is another milestone to achieve, which in turn, leads to more durability and wear resistance.[15–17]

The application of surface engineering techniques is found to be an effective strategy for either solving problems associated with NiTi or inducing new properties into its surface.[18] To date, a variety of strategies, including magnetron sputtering, sol–gel, and spraying, have been utilized to modify the NiTi surface. Various ceramics, *e.g.*, CaP and transition metal oxides (TiO_2 and ZrO_2), as well as polymers, such as chitosan, polylactic acid, and polypyrene, are potential coating materials used to attain superior properties or address the facing limitations of NiTi.[19–22] The deposition of the CaP family layer on NiTi is a key solution to suppress Ni ion leaching, improve antibacterial performance, and increase bioactivity. On the other hand, there is a dire need to strengthen the brittle nature of CaP ceramics to obtain more tough coatings with the desired stiffness. Meanwhile, a new challenge, namely poor bonding strength, emerges when applying a ceramic coating on the metallic substrate.[23–29] The recent progress in surface engineering offers the exploitation of constructive properties of the reinforcing agents to solve this problem. The reported results have demonstrated the positive role of ceramic reinforcing particles, *e.g.*, ZnO and TiO_2, in promoting the mechanical properties of the HAp electrodeposits.[30,31] The type and concentration of the included reinforcing phase can seriously alter the mechanical properties of the HAp films. It is to be emphasized that the added phase should not degrade the biological performance of the films. Nb_2O_5 particles seem to be an appropriate candidate to promote the tribomechanical properties and biocompatibility of the electrodeposited HAp coatings due to their illustrious resistance against both wear and corrosion, high stability, magnificent mechanical strength (elastic modulus of over 100 GPa), and striking bioactivity and biocompatibility.[32–36]

A survey of the literature demonstrates that there is no empirical work focusing on the role of Nb_2O_5 reinforcing agents on the tribomechanical performance of HAp electrodeposits. Following the gap in previous studies, we have attempted to address the effect of the concentration of the dispersed Nb_2O_5 particles in the bath on tribomechanical performance and the *in vitro* biocompatibility of the HAp coatings. It is believed that the proposed strategy will be helpful in minimizing the stress-shielding of NiTi and improving HAp/NiTi adhesion strength without a fall in the biocompatibility of HAp-coated NiTi.

2. Materials and methods

2.1. Electrolyte preparation and electroplating process

NiTi (Ni 50.2%–Ti 49.8%) disks with a diameter of 1 cm and thickness of 1 mm were used as working electrodes. The density, surface roughness, hardness, and elastic modulus of the used NiTi are 6.45 g cm^{-3}, 10 nm, 3.3 GPa, and 38 GPa, respectively. The pre-treatment protocol of the NiTi substrates, electrolyte composition, and electrodeposition parameters have been provided in our previous work,[37] schematically illustrated in Fig. 1.

The coatings produced by 0, 0.25, 0.50, and 1.0 g L^{-1} of Nb_2O_5 particles in the electrolyte will be labeled S1, S2, S3, and S4, respectively, in the following text (see Table 1). The Nb_2O_5 particles were added in the range of 0–1 g L^{-1}. A further rise in the concentration of the particles in the electrolyte led to severe agglomeration of the particles in the microstructure of the layer and the deposition of an uneven coating. Moreover, it is difficult to maintain this high number of Nb_2O_5 particles suspended in the electrolyte due to their high density.

2.2. Characterization

The phase composition of the electroplated coatings was evaluated by GIXRD using Cu-Kα radiation (Bruker D8 Advance, Germany). The patterns were collected at the incidence angle of $1°$ in the 2θ range of 5–85°. The crystallite size of the electrodeposited coatings was calculated through the Scherrer formula as follows:[38]

$$D = \frac{k\lambda}{\beta \cos \theta} \tag{1}$$

where k, λ, β, and θ are the Scherer constant, X-ray wavelength, FWHM of peak, and Bragg angle, respectively.

The surface and cross-sectional morphology of the produced coatings were assessed using a FESEM (MIRA3 TESCAN, Czech Republic).

The elemental composition and chemical states of the outermost and subsurface layers were studied *via* XPS (Thermo Fisher Scientific K-Alpha, USA) using an Al Kα source. To study the subsurface layers, a uniform etching process was carried out by a rastered Ar$^+$ beam under the voltage of 4 keV at a rate of approx. 0.25 nm s^{-1} for 240 s. The hydrocarbon C 1s at a binding energy of 284.6 eV was selected as a reference in processing the XPS data.

The surface wettability was measured using the sessile drop method with a static/dynamic contact angle measurement device (KSV CAM200, KSV Instruments, Finland) at 25 ± 1 °C. The presented values are the average of three various measurements.
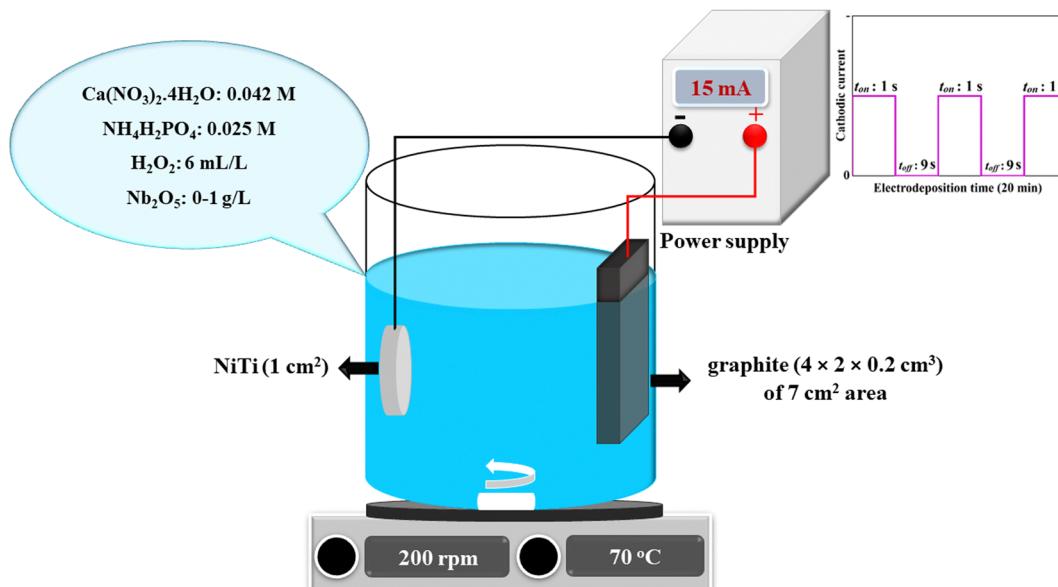
Fig. 1 Schematic illustration of the electrolyte composition and electrodeposition parameters in the present work.

Table 1 Labeling electrodeposited coatings based on the Nb_2O_5 level in the electrolyte

Label	Nb_2O_5 level in the electrolyte (g L^{-1})
S1	0
S2	0.25
S3	0.50
S4	1.0

2.3. Mechanical behavior

The nanoindentation apparatus (Agilent G200, AGILENT Technologies Inc., CA, USA) with a Berkovich diamond tip was used to measure the hardness and elastic modulus of the electroplated coatings. The Oliver-Pharr method allowed automatic calculation of the hardness and elastic modulus value using the nanoindentation tester. The nanoindentation assay was performed in the load-control mode. The maximum load was 5 mN with a constant loading rate of 0.5 mN s^{-1}. When it reached the maximum load, the loading was held for 5 s. The reported values are the mean of 15 separate measurements.

The adhesion strength between the developed composite films and NiTi substrate was measured by the pull-off test according to the ASTM F1044-05 standard under a constant strain rate of 1 mm min^{-1} (a schematic of the pull-off test is presented in the ESI,† Fig. S1).[39] The tensile strength of the used glue was 50 MPa.

The adhesion strength and tribological properties of the coatings were evaluated using the nanoscratch technique. The prepared coatings were subjected to scratching using the CSM nanoscratch tester (CSM Instruments, actual Anton Paar, Switzerland). A diamond tip with a diameter of 20 μm was employed to apply a normal load (FN) in the progressive mode. The scratch length was 1 mm, and the lateral scratch speed was maintained at 0.5 mm min^{-1}. To determine the critical normal load of initial cracking (L_c), the following test parameters were employed: an initial load of 0.3 mN, a final load of 100 mN, and a loading/unloading rate of 49.85 mN min^{-1}. The variations in normal force (Fn), frictional force (Ft), and frictional coefficient with the scratch distance were recorded using Scratch V4.52 software, along with the optical panorama image of the surface deformation after the scratch.

2.4. In vitro biocompatibility

2.4.1. Cell culture and seeding.
The mouse fibroblast cell line NIH3T3 was utilized to evaluate the *in vitro* biocompatibility of the specimens. The cells were cultured in DMEM high glucose, supplemented with 10% bovine calf serum, 1% L-glutamine, and 1% antibiotics. The cultured cells were maintained in a humidified 5% CO_2 incubator at 37 °C. The cell detachment process was carried out when they reached confluency. The samples were sterilized before the cells were seeded on them. Details of the sterilization process are reported in our previous paper.[32] The sterilized specimens were located in a 12-well cell culture plate, then the cells with a density of 2×10^5 cells per mL were seeded on their surface.

2.4.2. Cell adhesion and viability.
The cell viability was studied using the MTT colorimetric assay (Sigma-Aldrich, St. Louis, SM, United States) at 1, 3, and 7 days after cell seeding. MTT solution (5 mg mL^{-1}), dissolved in sterile PBS (0.134 M NaCl, 20 mM Na_2HPO_4, 20 mM NaH_2PO_4), was used as a stock solution at a working concentration of 0.5 mg mL^{-1}. The colorimetric reaction was analyzed by CLARIOstar (BMG Labtech, Ortenberg, Germany) at a 570 nm wavelength with 630 nm as the reference wavelength. All of the viability assays were performed in triplicate and repeated 2 times.

2.4.3. Confocal laser scanning microscopy (CLSM).
For CLSM observations, the 24 h cell-seeded samples were removed from the incubator and washed with PBS. In the next step, the

cells were fixed by the addition of 4% (w/v) PFA solution for 30 min at 4 °C. Then, they were permeabilized with 0.1% Triton X-100 for 5 min. Hoechst 33 342 (2 µg mL^{-1}) was used for nuclei staining. To visualize the F-actin cytoskeleton organization, cells were stained with tetramethylrhodamine B isothiocyanate (TRITC) phalloidin conjugate solution (10 µg mL^{-1}, EX/EM maxima $\approx$ 540/575, Sigma-Aldrich) in PBS for 40 min at RT. The CLSM images were obtained using a TCS SP8 confocal microscope (Leica Microsystems, Bensheim, Germany) equipped with a digital image capture system at 20× magnification.

2.4.4. Cell morphology determined using SEM. The morphology of the cells on the samples was studied using SEM after 7 days of incubation. For this purpose, the cells were fixed with a 2.5% (v/v) glutaraldehyde solution (Sigma Aldrich, St. Louis, MO, USA) in 0.1 M sodium cacodylate buffer (pH 7.2) for 1 h at 4 °C. The samples were washed twice with Na-cacodylate to remove excess glutaraldehyde, then they were dehydrated using increasing concentrations of ethanol (25, 50%, 75%) (Merck Life Science S. r.l, Milano, Italy) for 7 min and two washes of 96% ethanol for 15 min. The samples were lyophilized for 3 h using K-850 apparatus (Emitech Ltd, Ashford, UK) and placed on a mounting base. The cell morphology images were acquired using a SEM (Zeiss EVO-MA10, Oberkochen, Germany).

2.5. Statistical analysis

Statistical analysis was carried out *via* GraphPad Prism version 9.0 (GraphPad, Inc., San Diego, CA, USA). Analysis was performed by one-way or two-way ANOVA analysis of variance (ANOVA), followed by the Bonferroni *post hoc* test (significance level of 0.05).

3. Results and discussion

3.1. Phase structure

The GIXRD patterns of the studied specimens are illustrated in Fig. 2. While the phase composition of sample S1 consists of HAp diffraction (JCPDS card No. 09-0432), the phase structure of the S2, S3, and S4 coatings comprises HAp, Nb_2O_5 (JCPDS card No. 16-0053), and a trace amount of DCPD (JCPDS card No. 9-0077) phases. A weak peak emerged at $2\theta \approx 11°$ corresponding to DCPD, which is the precursor of the HAp phase.[40] It has been shown that the presence of this phase, at low amounts, besides HAp, is beneficial for improved *in vivo* biomineralization and biocompatibility.[32]

The incorporation of the particles into the growing layers led to the appearance of a new HAp peak, *e.g.*, $2\theta \approx 42°$, indicating that the included particles served as heterogeneous nucleation sites. A decrease in the crystallite size of the composite films, presented in Table 2, is another observation that approves the positive role of the included particles in providing extra nucleation sites. Moreover, the rapid nucleation rate during the deposition of the composite films, resulting from the presence of Nb_2O_5 particles, is responsible for the incomplete transformation of DCPD to HAp. The presence of enough hydroxyl ions together with enough time are two required factors for the mentioned transformation.[32] The reason for the presence of strong Nb_2O_5 diffractions is using an X-ray beam with a low incident angle, which determines the phase structure of the outermost layers of the coatings.

The strong HAp peak at $2\theta \approx 26°$ with the crystal face of (002) reveals that the crystals preferentially grow in the direction of the *c*-axis, namely perpendicular to the NiTi substrate.
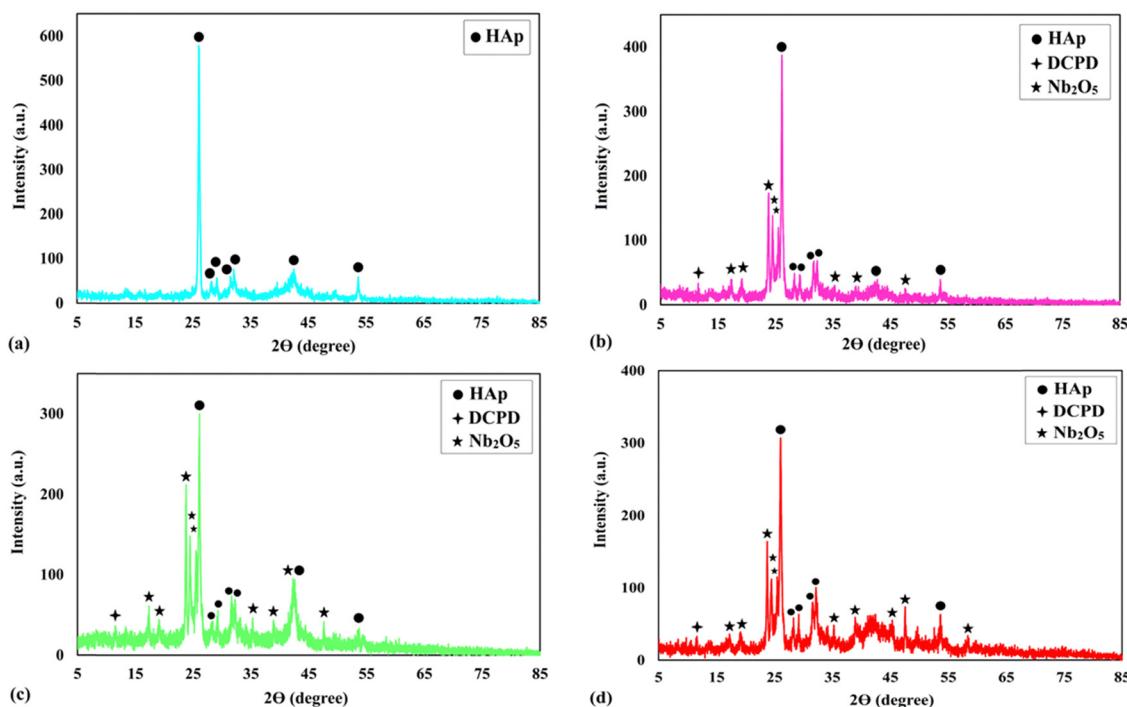

Fig. 2 The GIXRD patterns of the studied specimens: (a) S1, (b) S2, (c) S3, and (d) S4.

Table 2 The crystallite size of the coatings calculated through the Scherrer formula

Material type	Crystallite size (nm)
S1	91
S2	54
S3	51
S4	56

The intensity of the main HAp peak at $2\theta \approx 26°$ was significantly reduced for samples S2–S4. The following equations were used to quantify the preference of the crystals to grow along the c-axis[41]:

$$\text{RI} = \frac{I_{(002)}}{I_{(211)} + I_{(112)} + I_{(300)}} \qquad (2)$$

$$P = \text{RI} - \frac{\text{RI}_s}{\text{RI}} \qquad (3)$$

where P is the preference, RI is the preferred relative intensity, and RI_s is 0.182, obtained from the relative strength of the c-axis in standard PDF cards.[42] Fig. 3 shows the changes in preference degrees of the electrodeposited coatings to grow along the c-axis. It is obvious that the P value drastically decreases with the incorporation of the reinforcing phase.

Overall, HAp crystals grow along the a-, b-, and c-axes. The growth units on the a- and b- axes are OH–Ca$_6$ coordination cations, while the growth on the c-axis occurs on coordination anions Ca–P$_6$O$_{24}$. Ca–P$_6$O$_{24}$ is the most stable growth element, therefore, HAp crystals thermodynamically prefer to grow along the c-axis. The amount of OH$^-$ ions is the critical factor in increasing the tendency of the crystals to be grown along the c-axis. Since the included particles enhance the kinetics of the nucleation process, which consumes a higher concentration of the OH$^-$ ions, there are not sufficient ions that can support growth through the c-axis.[43,44] Therefore, a descending trend is seen for the P value of the composite samples.

3.2. Surface characteristics

The FESEM top-view micrographs of the studied specimens are indicated in Fig. 4. The particle morphology of the porous S1
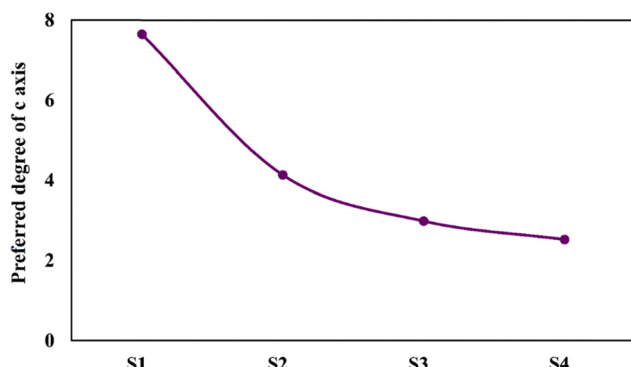

Fig. 3 The preference degrees of the electrodeposited coatings to grow along the c-axis.
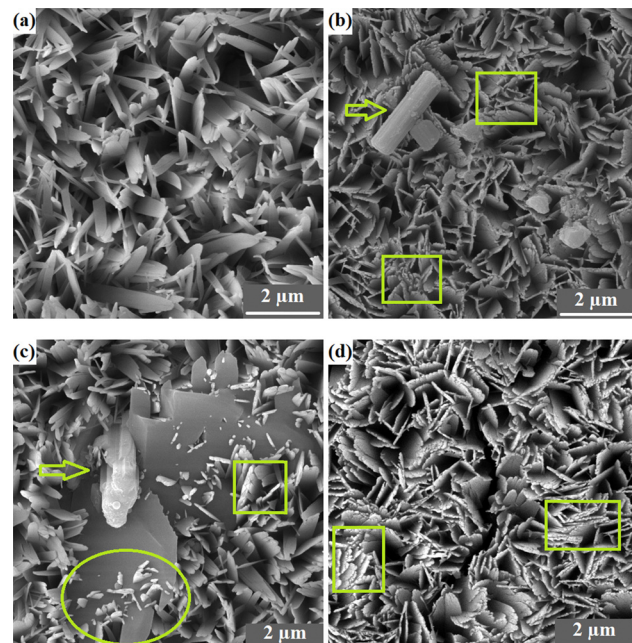
Fig. 4 FESEM top view micrographs of the studied specimens: (a) S1, (b) S2, (c) S3, and (d) S4.

sample is needle-like. A change in the particle morphology from needle-like to plate-like is obvious with the inclusion of the particles in the HAp matrix. It is to be mentioned that there are still some needle-like crystals throughout the surface of the composite layers. The incorporated particles, shown by arrows, are both placed between the growing crystals and located on the surface. In general, a more compact surface was obtained with the addition of the reinforcing Nb$_2$O$_5$ particles, as shown by the rectangles in Fig. 4b–d. The S3 sample has the most compact surface.

The nucleation of new HAp crystals over the existing HAp plates is indicated by the oval in Fig. 4c. The FESEM cross-sectional images of the samples obtained using both SE and BSE are exhibited in Fig. 5.

The images confirm the formation of an appropriate bond between the substrate and coatings without any flaws, cracks, or other defects. The thickness of the S1, S2, S3, and S4 coatings is 14.5, 11.5, 11, and 10 μm, respectively. A decrease in thickness with the inclusion of the reinforcing particles may be attributed to the formation of a more compact microstructure and the low preference for growth along the c-axis.[45,46] The XPS survey spectra of the outermost and subsurface layers and the data extracted from the spectra are presented in Fig. 6.

The XPS survey spectrum of the S1 sample comprises Ca 2p, P 2p, and O 1s peaks, as the main precursors of HAp structure, along with a C 1s peak, originating from the dissolving of the atmospheric CO$_2$ in the plating bath.[47] Besides the mentioned regions, there is an additional Nb 3d region in the XPS spectra of the S2–S4 samples, which is assigned to the presence of Nb$_2$O$_5$ throughout the surface of the composite films. The binding energy values of Ca 2p$_{3/2}$, P 2p$_{3/2}$, O 1s, and Nb 3d$_{5/2}$ peaks are 346.9, 132.5, 530.7, and 206.5 eV, respectively.
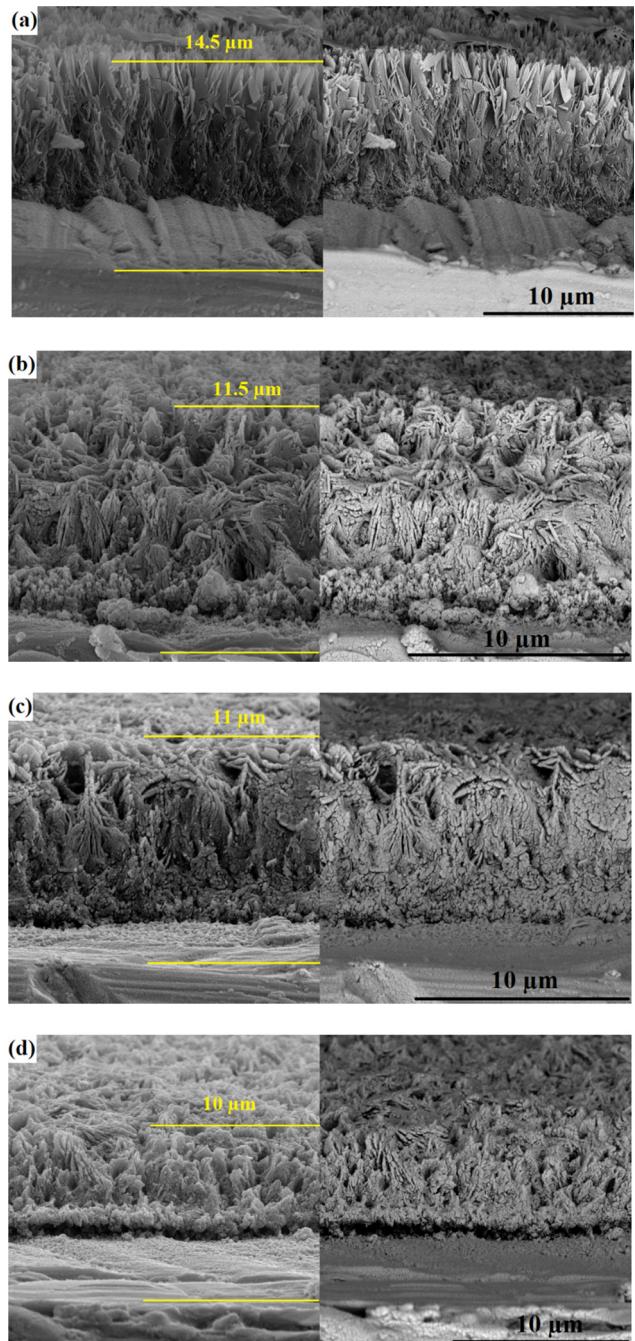
Fig. 5 The FESEM cross-sectional images of the samples obtained using both SE and BSE: (a) S1, (b) S2, (c) S3, and (d) S4.

The obtained binding energy values of Ca $2p_{3/2}$ and P $2p_{3/2}$ comply well with the energies of Ca–O and P–O bonds in standard HAp.[48] Moreover, the binding energy value of O 1s matches the energy of hydroxyl ions existing in the HAp structure and oxide species.[47] The XPS high-resolution spectra of Ca 2p, P 2p O 1s, and Nb 3d regions in the S3 sample are exhibited in the ESI,† Fig. S2. The data presented in Fig. 6a) reveal that the Ca/P molar ratio of the samples is in the range of 1.27–1.33. The Ca/P ratio in the precursor powders is 1.67; however, the Ca/P molar ratio of the outermost surface of the

coatings is in the range of 1.27–1.33. A decrease in the Ca/P ratio can be attributed to the dissolution of the atmospheric carbon in the aqueous electrolyte. The application of the etching treatment led to an increase in the Ca/P, where the ratio is in the range of 1.42–1.46. The reported results in the literature confirm that the Ca/P ratio of the natural bone, measured by the XPS, is 1.42 ± 0.02,[49] which is in agreement with the data presented in this work. It is to be mentioned that there is no obvious change in the binding energies of the various regions after the etching treatment. A statistically significant decrease in the C content of the coatings is observed with the etching process. Similar results have been reported by Ohtsu *et al.*[50] On the other hand, the Nb content increases with the etching, which demonstrates the presence of the reinforcing phase throughout the thickness of the film. In summary, it can be concluded that the chemical composition of the outermost and subsurface layers is similar to that of the bone.

The results of contact angle measurements using SBF drop are presented in Fig. 7. The applied surface modification technique resulted in a more hydrophilic surface. The (i) polar OH groups of the top HAp layer and (ii) ionic character of the deposited ceramic coating led to an increase in the wettability of NiTi.[32] The contact angle between the SBF drop and the coated samples increased with the inclusion of the Nb_2O_5 particles due to the fact that the particles regionally prevented the water molecules from penetrating the surface. Optimizing surface wettability is a key strategy to achieving the most appropriate biological responses. This means that moderate hydrophilicity, in the range of 20–40°, is needed for improved cell-material interactions.[51,52] The composite samples provide a favorable substrate for the adhesion and proliferation of the eukaryotic cells in terms of surface hydrophilicity.

3.3. Tribomechanical performance

The mechanical properties of a synthetic implant, especially hardness and elastic modulus, are very important in orthopedics for load-bearing applications since the material may undergo friction and stresses *in vivo*. In fact, a poor mechanical behavior of the coatings leads to the rapid dissolution of the coating. For analyzing the mechanical properties of brittle ceramics, the nanoindentation test bears some advantages over the other characterization methods as the nanoindentation results are more reliable in the nanoscale, and it gives a perspective about the overall properties, such as elastic modulus, hardness, and mechanical strength.[5,53] The load–displacement curves of the electrodeposited specimens are shown in Fig. 8. The extracted data from the curves are outlined in Table 3. The lower the indentation depth, the higher the hardness is.[54] From the curves, it can be deduced that the S4 sample has the highest hardness. The reason why the load–displacement curve of the S1 sample shows a large plateau-like behavior in the range of 0–700 nm is attributed to the high amount of porosity over the surface so that the indenter runs throughout the surface to reach the maximum load.[31] The presence of several discontinuities in the load–displacement curves, in particular for the S1 sample, can be interpreted by the crystals bending or cracking.[55] It is not
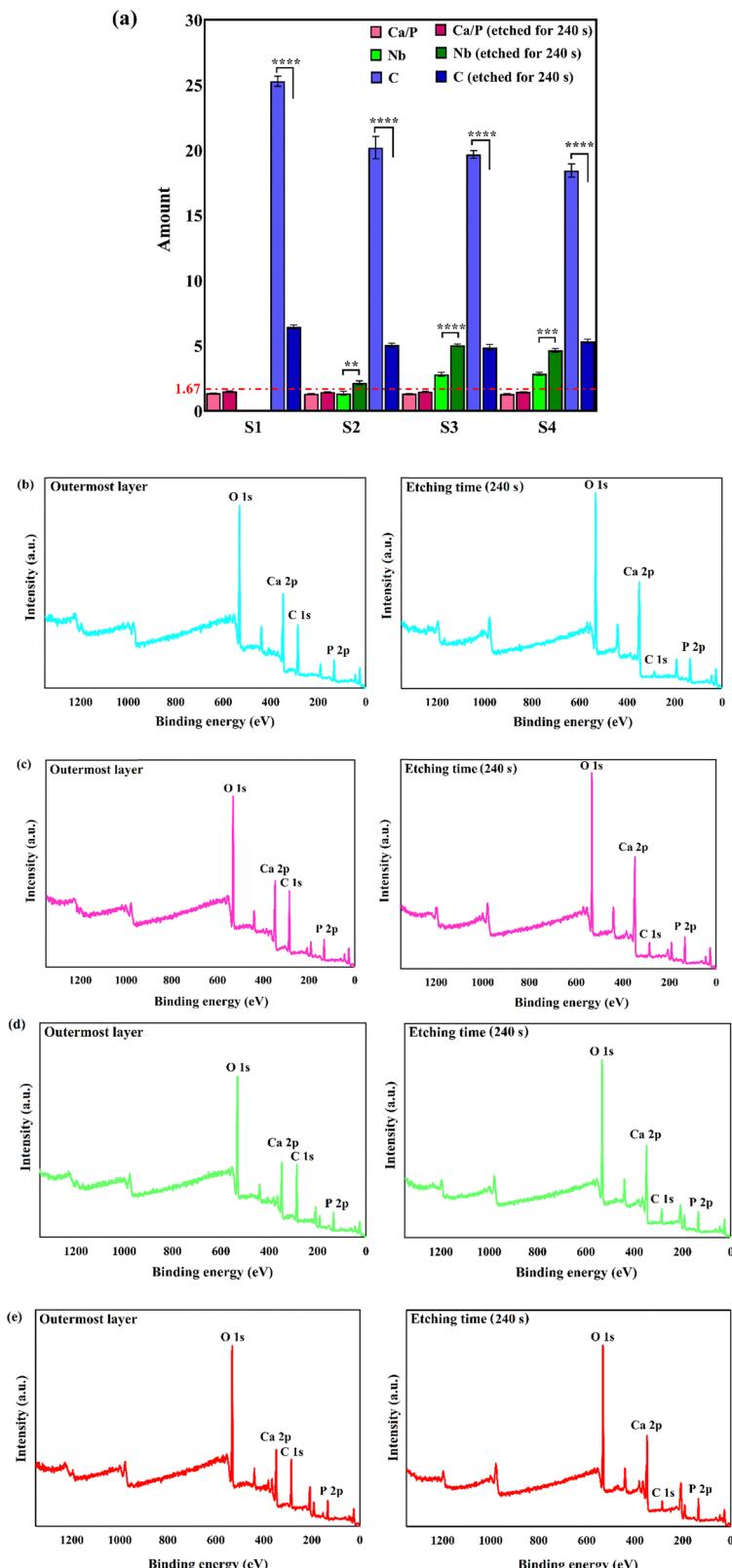
Fig. 6 (a) The XPS-derived data, including Ca/P ratio and atomic percent of Nb and C elements (**p = 0.0013, ***p = 0.0001, and ****$p < 0.0001$); and XPS survey spectra of the outermost and subsurface layers: (b) S1, (c) S2, (d) S3, and (e) S4.

surprising to see the pop-in and pop-out in the load–displacement diagrams of the layers as they are made of brittle HAp ceramic.

The pop-in phenomenon, where a sudden increase in indenter displacement occurs, is seen during the loading path of the
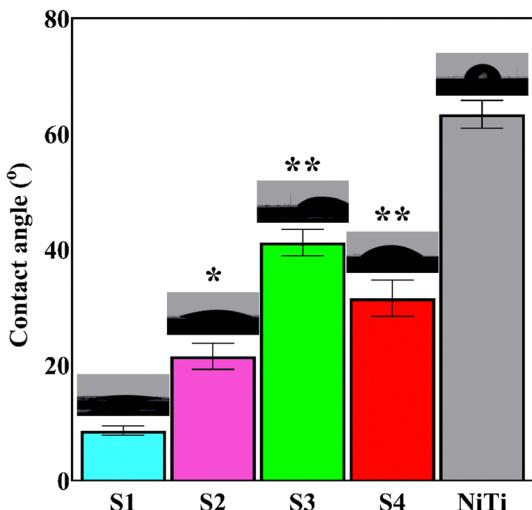
Fig. 7 Results of contact angle measurements using SBF drop (*p = 0.0001 and **$p < 0.0001$ vs. S1).
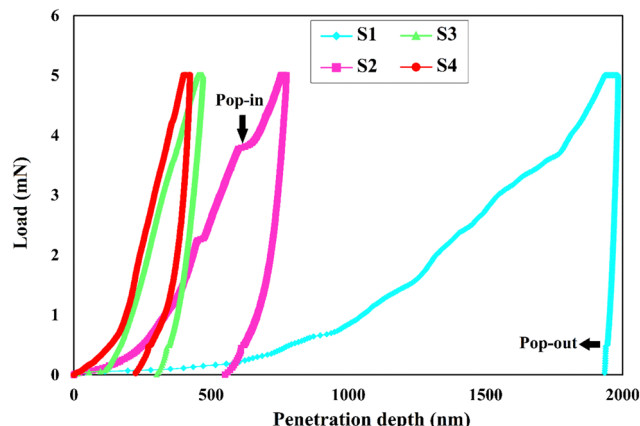

Fig. 8 The load–displacement curves of the electrodeposited specimens.

Table 3 The mechanical data extracted from the load–displacement curves. H, E, H/E, and H^3/E^2 are hardness, elastic modulus, resistance to elastic deformation, and resistance to plastic deformation, respectively. The H/E index is also the marker of fracture toughness and wear resistance of the material

Specimen type	H (GPa)	E (GPa)	H/E	H^3/E^2
NiTi	3.3 ± 0.13	38 ± 1.1	86.8×10^{-3}	24.88×10^{-3}
S1	0.05 ± 0.001	17.1 ± 0.6	2.92×10^{-3}	4.27×10^{-7}
S2	0.38 ± 0.01	17.3 ± 0.8	21.9×10^{-3}	1.83×10^{-4}
S3	1.15 ± 0.04	26.8 ± 1.1	42.9×10^{-3}	21.17×10^{-4}
S4	1.3 ± 0.06	43.9 ± 2.1	29.6×10^{-3}	11.39×10^{-4}

porous or crack-containing materials. The load–displacement curve of the S1 sample has the highest number of pop-ins due to its high porosity and micro-sized pores. The pop-in events can be categorized into three types depending on their length: (i) micro, (ii) moderate, and (iii) extreme. While the pop-in events

measured less than 10 nm and 100 nm in length fall under the micron and moderate classes, respectively, those with a length >100 nm are labeled extreme.[56] In general, the observed pop-ins in this work are micron and moderate. For instance, there is a moderate pop-in with a length of 25 nm in the load–displacement curve of the S2 sample, shown by an arrow.

The elastic deformation and plastic deformation energies are obtained by calculation of the corresponding areas in the load–displacement curve (see the ESI,† Fig. S3). The area surrounded by the loading curve and displacement axis, and that enclosed by the unloading curve and displacement axis, are assigned to elastic deformation and plastic deformation energies, respectively. In all of the specimens, the area corresponding to plastic energy is much larger than that of elastic energy, illustrating that the irreversible deformation was dominant as a result of the applied load.

To avoid the effect of substrate on the measured mechanical properties by the nanoindentation, the penetration depth should not exceed 10% of the coating thickness.[55] Bearing in mind the thickness of the composite layers, ranging from 10–11.5 μm, and the penetration depths, maximum 0.5 μm, it is obvious that the substrate has no influence on the measured properties. For the S1 sample, although the substrate may affect the properties, the obtained results confirm that the sample has a weaker mechanical performance than that of composite films, even with the contribution of the substrate. This also shows that the contribution of the substrate was negligible.

In general, a marked increase in the mechanical properties of the HAp coatings is obtained with the co-deposition of the Nb_2O_5 particles. There are potential factors, including smaller crystallite size, more compact surface, the high level of hardness and elastic modulus of the included Nb_2O_5 particles, favorable load-transfer between the reinforcing particles and the HAp matrix arising from the larger interface-volume ratio, and the plate-like particle morphology, governing the higher mechanical properties of the composite samples compared to the pure HAp one.[53,57] It was found that the plate-like morphology renders higher mechanical properties than that of the needle-like one due to decreased porosity.[53,55]

The potential toughening mechanisms of the pure HAp layer with the included Nb_2O_5 reinforcing phase are crack deflection, crack branching, and crack bridging. Once the crack reaches the Nb_2O_5 particles, it has to be branched or deflected to find a new propagation path, which takes much more energy.[58]

The hardness and elastic modulus of the cortical bone are 0.52–0.74 and 15–30 GPa, respectively.[31] The excellent match between the elastic modulus of the composite coatings, in particular S3 and the bone, along with the higher hardness of the coatings than that of bone, makes the developed coatings an excellent candidate for orthopedic applications. While the former lead to a decrease in implant loosening and an increase in stimulation of new bone formation, the latter eliminates the risk of coating demolition during the surgical procedure.[59] Additionally, the high mechanical behavior and durability of the biomedical coatings guarantee their excellent corrosion

protection efficiency. The published results on the improved corrosion performance of the HAp-Nb_2O_5 films by our research team approve such a claim.[37] Fornell *et al.*[55] measured the mechanical properties of electrodeposited HAp coatings from H_2O_2-containing electrolyte with a thickness of ≈ 14 μm using a nanoindentation test under the load of 5 mN and showed that the hardness and reduced elastic modulus of the coatings are 0.014 ± 0.004 and 3.1 ± 1.0 GPa, respectively.

Strong adhesion between the coating and the substrate ensures the efficient performance and durability of the coated biomaterial during/after implantation since the applied stresses can cause detachment of the coating from the substrate. Poor implant/coating adhesion is one of the main challenges facing the successful use of the electrodeposition technique in the surface finishing of biomaterials.[5,57] Fig. 9 shows the adhesion strength values of the coatings. According to the ISO 13779-2 standard, the minimum implant/coating bonding strength should be 15 MPa so that the system is qualified for use *in vivo*.[57] The results show that almost all of the developed systems meet the standard requirement. The NaOH alkali pre-treatment of NiTi, electrodeposition under pulsed current mode with a low duty cycle, and the application of moderate current density play a constructive role in achieving a strong bonding strength even for the S1 sample. The formation of a highly porous surface under high current densities due to the increased hydrogen evolution degrades the bonding strength, while at moderate current densities, the cohesive strength is dominant, leading to a failure at the interface of the coating/biomaterial.[60] Similarly, there are fewer H_2 bubbles generated during the pulsed current electroplating.[61] The bonding strength between the HAp top layer and the underlying NiTi substrate is enhanced with the inclusion of the Nb_2O_5 phase.

The synergistic role of cohesive strength and adhesive strength determines the overall adhesion strength. While the cohesive strength depends on crystallinity, porosity, and crack extension, the top layer/substrate interlocking, the mismatch between the elastic modulus of coating and substrate, and residual stress affect the adhesive strength.[62]

An increase in the coating density, decrease in CTE mismatch between the coating and implant, grain refinement, higher mechanical interlocking, and enhancement in the elastic modulus of the coatings (getting closer to that of NiTi), obtained by the inclusion of the particles, are the factors that promote the adhesive and cohesive strength. The CTE of NiTi, HAp, and Nb_2O_5 is 6.6×10^{-6}, 14×10^{-6}, and $5.3–5.9 \times 10^{-6}$ $1/k$, respectively.[63,64]

The adhesion strength between the S3 coating and the substrate is the highest, emphasizing the use of the optimum concentration of the reinforcements. Shojaee *et al.*[65] reported that the bonding strength between electrodeposited HAp and 316L stainless steel increased from 11.6 to 20.8 MPa with co-deposition of the 10 g L^{-1} of ZrO_2 particles; however, a further rise in the concentration up to 15 g L^{-1} degraded the strength.

Nanoscratch is a novel standard technique, rendering fruitful information on the coating/substrate adhesion strength and tribological properties of the coatings. The technique claims several advantages over the pull-off method, including (i) its ability to assess the shear stresses, which are more likely to occur in the human body during daily activities than tensile stress, and (ii) giving more accurate data. While the pull-off results are the sum of cohesive failure, adhesive failure and glue failure, the nanoscratch results only reveal the coating/substrate bonding strength.[31,66,67] Fig. 10 shows the obtained curves from nanoscratch testing along with the corresponding panorama images of track traces. The curves are divided into three regions: In the first region, shown by (I), there are no sharp fluctuations in the curves, where the diamond tip only touches the surface of the coating and slides over it. In the second region, indicated by (II), some significant fluctuations are observable, which illustrate the penetration of the tip in the coating. The third region, shown by (III), appears when the load has reached a certain level, indicating the serious plastic deformation of the coating.[66,68] Mokabber *et al.*[66] reported the absence of sudden changes in region II of the scratch curves of the electrodeposited calcium phosphate films, similar to those observed in the present work, which depict that the cohesive failure occurs without brittle delamination.

Critical load (L_c) is determined using typical scratch curves and/or panorama images of track traces. An abrupt increase in friction force and/or coating removal in scratch track corresponds to the critical load.[69] As shown, there are two L_c values for the studied coatings, indicating the gradual spallation of the coatings rather than sudden delamination. The latter takes place when there is one L_c.[70] The critical load values derived from the scratch test measurements are summarized in Table 4.

L_{c1} and L_{c2} refer to the cracking initiation and coating spallation, respectively.[70] The higher L_c value correlates with a higher adhesion strength. The presented data in Table 4 reveal an improvement in the L_c value of the S1 sample with the inclusion of the Nb_2O_5 strengthening phase. The nanoscratch
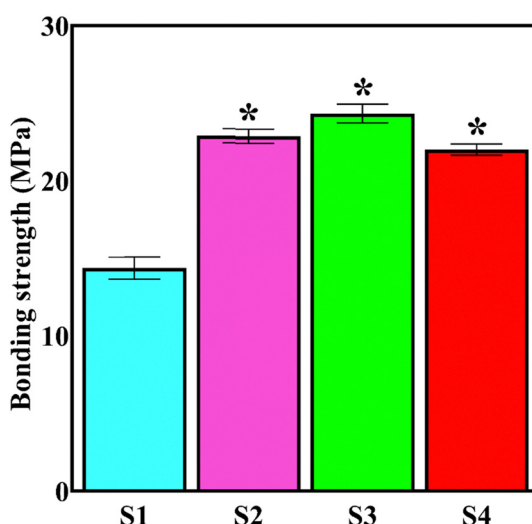

Fig. 9 Coating-substrate adhesion strength values (*$p < 0.0001$ *vs.* S1).
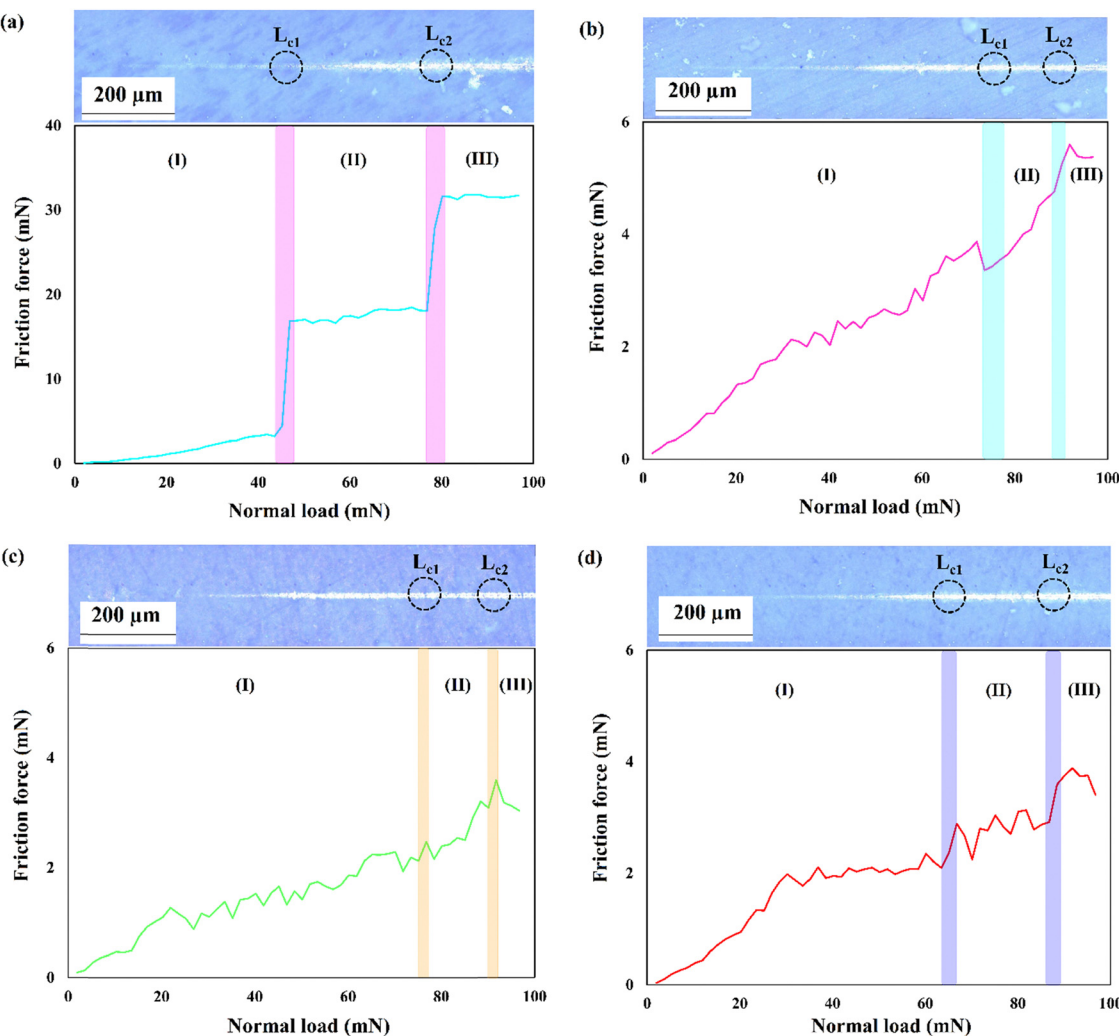
Fig. 10 Obtained curves from nanoscratch testing along with the corresponding panorama images of track traces (at the magnification of 100×): (a) S1, (b) S2, (c) S3, and (d) S4.

Table 4 The critical load values derived from the nanoscratch test measurements

Specimen	L_{c1} (mN)	L_{c2} (mN)
S1	45.1	76.7
S2	73.4	88.4
S3	76.7	90.0
S4	66.81	86.7

results comply with the results of the pull-off test, where S3 has the highest bonding strength due to its excellent surface and microstructural features. The published results demonstrate the increase in L_c value of HAp coating with the addition of the reinforcements. For instance, Mehrvarz et al.[31] reported that the L_c of the HAp electrodeposit increases from 58 to 91 mN with the addition of 0.4 g L^{-1} ZnO nanoparticles to the HAp electrolyte.

The panorama images of the scratch track demonstrate that there are no visible fracture signs inside/at the border of the scratch track, which is a marker of appropriate coating/

substrate bonding. In addition, the damage induced by the tip is limited to the contact area inside the coating.

The conventional pin-on-disk technique is not suitable for determining the tribological behavior of the brittle HAp coatings. The slope of the first region in the typical scratch curve, where the tip only slides over the surface, provides the COF values.[31,71] The COF-load curves obtained from the scratch test data are exhibited in the ESI,† Fig. S4. The COF varies in the range of 0–0.1, showing the favorable tribological and wear properties of the electrodeposited films. The mean COF values of the S1, S2, S3, and S4 samples are 0.058, 0.055, 0.038, and 0.042, respectively. The included particles partially act as solid-lubricant. The lower the COF value, the higher the wear resistance is. Moreover, the enhanced hardness of the Nb$_2$O$_5$-reinforced layers contributes to the higher wear resistance, in accordance with Archard's law.[72]

3.4. *In vitro* biocompatibility

The application of embryonic fibroblast cell lines (NIH3T3) has garnered great attention in biomedical fields since the

fibroblasts are mesenchymal cells of connective tissue, not only producing extracellular matrix components but also involved in cell cycle, tissue architecture, and wound and bone healing. These cells allow the assessment of the basal cytocompatibility of the synthetic implant from the viewpoint of cell viability, growth, proliferation, *etc.*, on its surface. The fibroblasts are the first cells attached to the implanted material. They produce immature collagen, which precipitates on the material. Overall, fibroblasts and osteoblasts are two types of cells that are in direct connection with the surface of the orthopedic implants.[73–76]

The outermost layer of the biomaterial decides its biological response *in vivo* since it is the first component that comes into contact with the surrounding cells and tissues. The beneficial role of the HAp-Nb$_2$O$_5$ composite layer on the *in vitro* biocompatibility of NiTi implants, determined by SAOS-2 osteoblastic cells, has been demonstrated in our previous work.[32] The results of the MTT assay and CLSM images of cell nuclei and
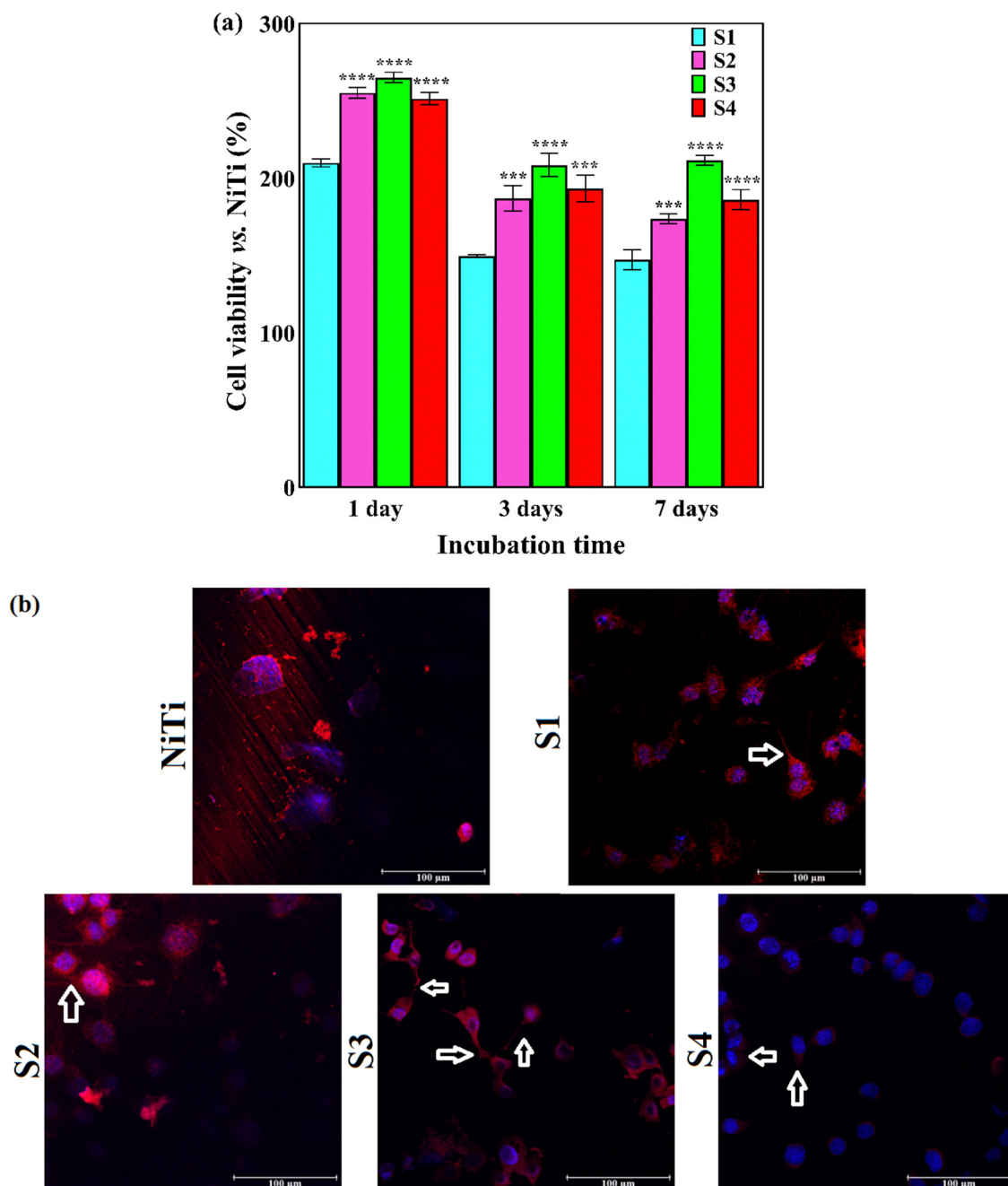

Fig. 11 (a) MTT results of NIH3T3 cell viability on the coated samples normalized to the bare NiTi (***$p < 0.0008$ and ****$p < 0.0001$ *vs.* S1) and (b) CLSM images of the NIH3T3 cells after 24 h of *in vitro* incubation, in which cell nuclei and actin filament are shown by blue fluorescence and red fluorescence, respectively. 100 μm scale bar.
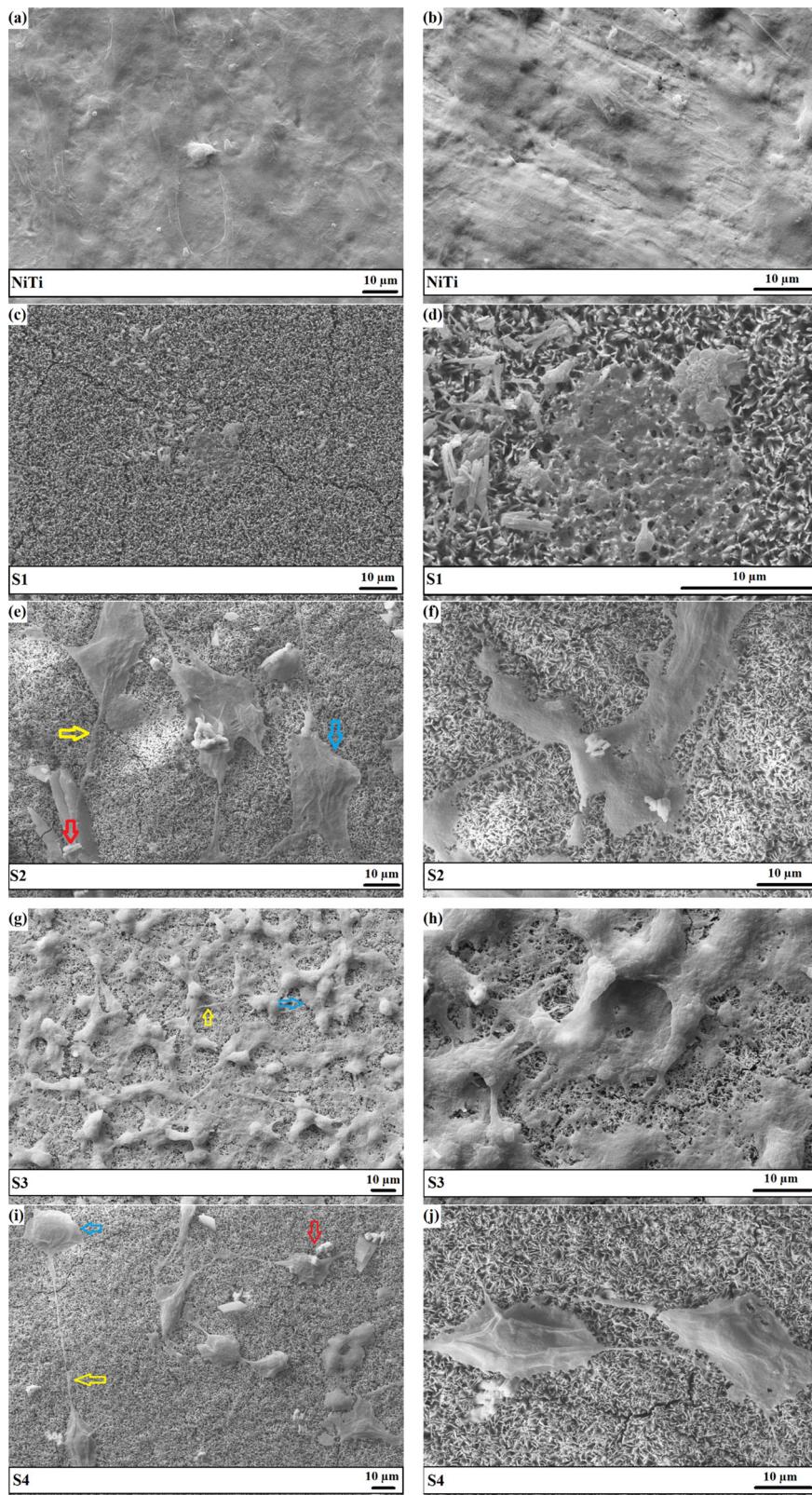
Fig. 12   Morphology of the NIH3T3 cells after 7 days of being cultured on the NiTi and coatings at various magnifications: (a) and (b) NiTi, (c) and (d) S1, (e) and (f) S2, (g) and (h) S3, and (i) and (j) S4. Yellow, blue, and red arrows indicate filopodia, lamellipodia, and Nb_2O_5 particles, respectively.

F-actin are illustrated in Fig. 11a and b, respectively. The applied surface modification strategy led to at least 200% increase in cell viability of the NIH3T3 cells within the first 24 h of incubation. Moreover, a significant difference in cell proliferation is observed for the composite coatings compared to the HAp one.

The adsorption of plasma proteins is the first stage in the formation of the protein layer, which serves as the interface for cell adhesion. The surface morphology, chemistry, wettability, and topography affect the protein adsorption rate.[32,77] The optimum surface wettability, porous surface, and presence of Nb_2O_5 particles are the contributing parameters for enhanced cell adhesion. It seems that the favorable surface characteristics of the Nb_2O_5-containing coatings provided a better substrate for NIH3T3 cell adhesion. The results confirm that the added Nb_2O_5 particles not only induce no toxicity but also promote cell functions. The NIH3T3 cell numbers on the bare and coated NiTi samples and the cell viability *versus* TCP after various incubation periods are indicated in the ESI,† Fig. SV and SVI, respectively. The cell proliferation for all of the studied coatings markedly increased during the incubation period. A material rendering cell viability >75% is considered non-cytotoxic in accordance with ISO 10993-5:1999.[78] All of the coated samples, in particular those reinforced by the Nb_2O_5 phase, provided higher viability than 75%, confirming their favorable biological responses.

Favorable cell adhesion is observable for all of the coated samples and may be due to the strong focal adhesions. There is a higher number of cells adhered to composite coatings compared with bare NiTi and S1 coating. The morphology of the overwhelming fraction of cell nuclei on the coatings is polygonal. The filopodia projections from cells, shown by arrows, are observable in the CLSM images of the coatings. The presence of filopodia demonstrates the beginning of the cell interactions with the substrate and surrounding cells within the first 24 h of incubation. There are a high number of long filopodia along with well-developed actin filaments in the CLSM image of S3, approving the accuracy of the MTT quantitative results. It is not possible to focus at high magnification *via* this microscope due to the high light reflection and pore topology. The morphology of the NIH3T3 cells after 7 days of being cultured on the NiTi and coatings is presented in Fig. 12. It is seen that the cultured NIH3T3 cells have different morphologies on the coatings. Cell colonies consisting of small globules are formed on the S1 sample (see Fig. 12d), while well-attached cells that spread over the surface with typical elongated shapes can be seen in SEM images of the S2–S4 samples. The fusiform and polygonal cell morphologies can also be observed in Fig. 12e–j. Fig. 12g indicates the formation of a confluent layer of the fibroblast cells that extends throughout the surface of the S3. The presence of filopodia and lamellipodia protrusions, marked by yellow and blue arrows, respectively, confirms the excellent adhesion of the cells to the surface and cell–cell contacts.[79] They are also responsible for cell migration and movement.[80] In summary, the S3 sample, benefiting from the most uniform surface with favorable hydrophilicity, the optimum

amount of Ca/P ratio and Nb_2O_5 particles, and the smallest crystallite size, offers the best *in vitro* compatibility with the NIH3T3 cells.

4. Conclusions

The present work has endeavored to evaluate the effect of Nb_2O_5 particle levels in the electrolyte, *i.e.*, 0–1 g L^{-1}, on the morphological, microstructural, tribomechanical, and biological performance of the HAp layers. The main results are drawn as follows:

•The phase structure of the particle-free coating consists mainly of the HAp phase. The addition of the particles led to the formation of trace amounts of DCPD and limited the crystal growth along the *c*-axis.

•A more compact surface with a favorable wettability for cell adhesion, in the range of 20–40°, is obtained with the incorporation of the Nb_2O_5 particles into the HAp matrix. There were no defects throughout the coating/substrate interface.

•The elemental composition of HAp-Nb_2O_5 throughout the outermost and subsurface layers was close to that of natural bone. The Nb content in the coatings was enhanced with an increase in particles level in the plating electrolyte.

•The addition of the Nb_2O_5 particles greatly improved the hardness, elastic modulus, and toughness of the HAp coatings. The high hardness and the favorable elastic modulus close to that of cortical bone reduce the risk of implant loosening and stress-shielding, respectively.

•The coating/implant bonding strength, studied by pull-off and nanoscratch, was promoted with the co-deposition of the reinforcing phase. Moreover, the COF of the composite coatings was lower than that of HAp coating due to the beneficial contribution of the Nb_2O_5 phase.

•The included Nb_2O_5 particles not only rendered a favorable platform for cell adhesion but also gave rise to cell functions, such as growth and proliferation.

•The developed HAp-Nb_2O_5 coating systems, in particular those electrodeposited from a bath containing 0.50 g L^{-1} Nb_2O_5, provided the best tribomechanical and biological properties. These coatings are believed to be successfully used for load-bearing orthopedics purposes.

Abbreviations

BSE	Backscattered electron
CLSM	Confocal laser scanning microscopy
COF	Coefficient of friction
CTE	Coefficient of thermal expansion
DCPD	Dicalcium phosphate dihydrate
DMEM	Dulbecco's modified Eagle's medium
ECM	Extracellular matrix
FESEM	Field emission scanning electron microscopy
FWHM	Full width at half maximum
GIXRD	Grazing incidence X-ray diffraction
HAp	Hydroxyapatite

MTT	3-(4,5-dimethylthiazol-2-yl)-2,5-diphenyl tetrazolium bromide
OCP	Octacalcium phosphate
PBS	Phosphate-buffered saline
PFA	Paraformaldehyde
SBF	Simulated body fluid
SE	Secondary electron
SEM	Scanning electron microscopy
TCP	Tissue culture plate

Conflicts of interest

There are no conflicts to declare.

Acknowledgements

References

1 M. Mozetič, *Materials*, 2019, **12**, 441.

2 R. Junker, A. Dimakis, M. Thoneick and J. A. Jansen, *Clin. Oral. Implants Res.*, 2009, **20**, 185–206.

3 S. Mohandesnezhad, M. Etminanfar, S. Mahdavi and M. S. Safavi, *Surf. Interfaces*, 2022, **28**, 101604.

4 S. Ahmadiyan, J. Khalil-Allafi, M. R. Etminanfar, M. S. Safavi and M. Hosseini, *Trans. IMF*, 2022, **100**, 93–102.

5 M. S. Safavi, M. A. Surmeneva, R. A. Surmenev and J. Khalil-Allafi, *Ceram. Int.*, 2021, **47**, 3031–3053.

6 N. Shokri, M. S. Safavi, M. Etminanfar, F. C. Walsh and J. Khalil-Allafi, *Mater. Chem. Phys.*, 2021, **259**, 124041.

7 A. Menazea, S. A. Abdelbadie and M. Ahmed, *Appl. Surf. Sci.*, 2020, **508**, 145299.

8 P. Zhao, Y. Liu, L. Xiao, H. Deng, Y. Du and X. Shi, *J. Mater. Chem. B*, 2015, **3**, 7577–7584.

9 J. Khalil-Allafi, H. Daneshvar, M. S. Safavi and V. Khalili, *Phys. B Condens. Matter*, 2021, **615**, 413086.

10 M. S. Safavi, A. Bordbar-Khiabani, J. Khalil-Allafi, M. Mozafari and L. Visai, *J. Manuf. Mater. Process*, 2022, **6**, 65.

11 M. S. Safavi, A. Bordbar-Khiabani, F. C. Walsh, M. Mozafari and J. Khalil-Allafi, *Curr. Opin. Biomed. Eng.*, 2023, **25**, 100429, DOI: 10.1016/j.cobme.2022.100429.

12 Y. Zhang, S. Attarilar, L. Wang, W. Lu, J. Yang and Y. Fu, *Int. J. Bioprinting*, 2021, **7**, 340.

13 D. Savio and A. Bagno, When the total hip replacement fails: A review on the stress-shielding effect, *Processes*, 2022, **10**, 612.

14 M. Zhang, T. Gregory, U. Hansen and C. K. Cheng, *J. Orthop. Res.*, 2020, **38**, 1566–1574.

15 L. Wang, J. Wang, Y. Xu, J. Zhu and W. Zhang, *Mech. Adv. Mater. Struct.*, 2022, 1–14, DOI: 10.1080/15376494.2022.2121990.

16 K. Kumar, A. Das and S. B. Prasad, *Mater. Today: Proc.*, 2021, **44**, 2038–2042.

17 T. Alonso, D. Favier and G. Chagnon, *J. Mater. Eng. Perform.*, 2019, **28**, 4667–4679.

18 R. Asghari, M. S. Safavi and J. Khalil-Allafi, *Trans. IMF*, 2020, **98**, 250–257.

19 R. A. Surmenev, M. A. Ryabtseva, E. V. Shesterikov, V. F. Pichugin, T. Peitsch and M. Epple, *J. Mater. Sci.: Mater. Med.*, 2010, **21**, 1233–1239.

20 D. Qiu, A. Wang and Y. Yin, *Appl. Surf. Sci.*, 2010, **257**, 1774–1778.

21 D. P. Aun, M. Houmard, M. Mermoux, L. Latu-Romain, J. C. Joud, G. Berthomé and V. T. Buono, *Appl. Surf. Sci.*, 2016, **375**, 42–49.

22 M. S. Safavi, J. Khalil-Allafi, E. Restivo, A. Ghalandarzadeh, M. Hosseini, G. Dacarro, L. Malavasi, A. Milella, A. Listorti and L. Visai, *Sci. Rep.*, 2023, **13**, 16045.

23 Y. Guo, Z. Xu, M. Liu, S. Zu, Y. Yang, Q. Wang, Z. Yu, Z. Zhang and L. Ren, *J. Mater. Res. Technol.*, 2022, **17**, 622–635.

24 Y. L. Lai, P. Y. Cheng, C. C. Yang and S. K. Yen, *Thin Solid Films*, 2018, **649**, 192–201.

25 K. Dudek, M. Dulski, T. Goryczka and A. Gerle, *Ceram. Int.*, 2018, **44**, 11292–11300.

26 M. E. Aksoy, B. Aksakal, N. Aslan and B. Dikici, *J. Mater. Eng. Perform.*, 2021, **30**, 7365–7375.

27 Y. Say and B. Aksakal, *J. Mater. Res. Technol.*, 2020, **9**, 1742–1749.

28 E. Mohseni, E. Zalnezhad and A. R. Bushroa, *Int. J. Adhes. Adhes.*, 2014, **48**, 238–257.

29 W. S. Harun, R. I. Asri, J. Alias, F. H. Zulkifli, K. Kadirgama, S. A. Ghani and J. H. Shariffuddin, *Ceram. Int.*, 2018, **44**, 1250–1268.

30 D. Qiu, L. Yang, Y. Yin and A. Wang, *Surf. Coat. Technol.*, 2011, **205**, 3280–3284.

31 A. Mehrvarz, J. Khalil-Allafi, A. Motallebzadeh and V. Khalili, *Ceram. Int.*, 2022, **48**, 35039–35049.

32 M. S. Safavi, J. Khalil-Allafi and L. Visai, *Biomater. Adv.*, 2023, **150**, 213435, DOI: 10.1016/j.bioadv.2023.213435.

33 P. Amaravathy, S. Sowndarya, S. Sathyanarayanan and N. Rajendran, *Surf. Coat. Technol.*, 2014, **244**, 131–141.

34 Y. Li, K. S. Munir, J. Lin and C. Wen, *Bioact. Mater.*, 2016, **1**, 127–131.

35 M. S. Safavi, F. C. Walsh, L. Visai and J. Khalil-Allafi, *ACS Omega*, 2022, **7**, 9088–9107.

36 O. Shcherbina, M. Palatnikov and V. Efremov, *Inorg. Mater.*, 2012, **48**, 433–438.

37 M. S. Safavi, J. Khalil-Allafi, I. Ahadzadeh, F. C. Walsh and L. Visai, *Surf. Coat. Technol.*, 2023, **470**, 129822.

38 T. C. Paul and J. Podder, *Appl. Phys. A: Mater. Sci. Process.*, 2019, **125**, 818.

39 M. Hosseini, J. Khalil-Allafi, M. Etminanfar, M. S. Safavi, N. Bloise and A. Ghalandarzadeh, *Mater. Chem. Phys.*, 2023, **293**, 126899.

40 X. Chu, W. Jiang, Z. Zhang, Y. Yan, H. Pan, X. Xu and R. Tang, *J. Phys. Chem. B*, 2011, **115**, 1151–1157.

41 D. He, X. Zhang, P. Liu, X. Liu, X. Chen, F. Ma, W. Li, K. Zhang and H. Zhou, *Surf. Coat. Technol.*, 2021, **406**, 126656.

42 M. C. Barbosa, N. R. Messmer, T. R. Brazil, F. R. Marciano and A. O. Lobo, *Mater. Sci. Eng. C*, 2013, **33**, 2620–2625.

43 Y. Zhu, L. Xu, C. Liu, C. Zhang and N. Wu, *AIP Adv.*, 2018, **8**, 085221.

44 P. Wang, C. Li, H. Gong, X. Jiang, H. Wang and K. Li, *Powder Technol.*, 2010, **203**, 315–321.

45 T. T. Nguyen, N. T. Pham, T. T. Dinh, T. T. Vu, H. S. Nguyen and L. D. Tran, *Adv. Polym. Technol.*, 2020, 1–10, DOI: 10.1155/2020/8639687.

46 N. T. Thom, P. T. Nam, N. T. Phuong, C. T. Hong, N. Van Trang, N. T. Xuyen and D. T. Thanh, *Vietnam J. Sci. Technol.*, 2017, **55**, 706–715.

47 M. E. El-Naggar, O. A. Ali, D. I. Saleh, M. A. Abu-Saied, M. K. Ahmed, E. Abdel-Fattah and S. F. Mansour, *J. Inorg. Organometallic Polym. Mater.*, 2022, **32**, 399–411.

48 N. Lowry, M. Brolly, Y. Han, S. McKillop, B. J. Meenan and A. R. Boyd, *Ceram. Int.*, 2018, **44**, 7761–7770.

49 H. B. Lu, C. T. Campbell, D. J. Graham and B. D. Ratner, *Anal. Chem.*, 2000, **72**, 2886–2894.

50 N. Ohtsu, S. Hiromoto, M. Yamane, K. Satoh and M. Tomozawa, *Surf. Coat. Technol.*, 2013, **218**, 114–118.

51 M. Steinerova, R. Matejka, J. Stepanovska, E. Filova, L. Stankova, M. Rysova, L. Martinova, H. Dragounova, M. Domonkos, A. Artemenko and O. Babchenko, *Mater. Sci. Eng. C*, 2021, **121**, 111792.

52 S. Tang, B. Tian, Y. J. Guo, Z. A. Zhu and Y. P. Guo, *Surf. Coat. Technol.*, 2014, **251**, 210–216.

53 M. Bartmanski, A. Zielinski, B. Majkowska-Marzec and G. Strugala, *Ceram. Int.*, 2018, **44**, 19236–19246.

54 M. R. Hosseini, M. Ahangari, M. H. Johar and S. R. Allahkaram, *Mater. Lett.*, 2021, **285**, 129097.

55 J. Fornell, Y. P. Feng, E. Pellicer, S. Suriñach, M. D. Baró and J. Sort, *J. Alloys Compd.*, 2017, **729**, 231–239.

56 S. S. Kasyap and K. Senetakis, *Materials*, 2021, **14**, 4579.

57 M. S. Safavi, F. C. Walsh, M. A. Surmeneva, R. A. Surmenev and J. Khalil-Allafi, *Coatings*, 2021, **11**, 110.

58 A. Janković, S. Eraković, M. Mitrić, I. Z. Matić, Z. D. Juranić, G. C. Tsui, C. Y. Tang, V. Mišković-Stanković, K. Y. Rhee and S. J. Park, *J. Alloys Compd.*, 2015, **624**, 148–157.

59 A. Fomin, M. Fomina, V. Koshuro, I. Rodionov, A. Zakharevich and A. Skaptsov, *Ceram. Int.*, 2017, **43**, 11189–11196.

60 Y. Han, T. Fu, J. Lu and K. Xu, *J. Biomed. Mater. Res.*, 2001, **54**, 96–101.

61 D. Khazeni, M. Saremi and R. Soltani, *Ceram. Int.*, 2019, **45**, 11174–11185.

62 D. Gopi, E. Shinyjoy, M. Sekar, M. Surendiran, L. Kavitha and T. S. Kumar, *Corros. Sci.*, 2013, **73**, 321–330.

63 S. Saber-Samandari, C. C. Berndt and K. A. Gross, *Acta Biomater.*, 2011, **7**, 874–881.

64 A. Hassan, S. Naga and M. Awaad, *Int. J. Refract. Met. Hard Mater.*, 2015, **48**, 338–345.

65 P. Shojaee and A. Afshar, *Surf. Coat. Technol.*, 2015, **262**, 166–172.

66 T. Mokabber, Q. Zhou, A. I. Vakis, P. Van Rijn and Y. T. Pei, *Mater. Sci. Eng., C*, 2019, **100**, 475–484.

67 M. Bartmański, L. Pawłowski, A. Mielewczyk-Gryń, G. Strugała, K. Rokosz, S. Gaiaschi, P. Chapon, S. Raaen and A. Zieliński, *Materials*, 2021, **14**, 1638.

68 S. Liu, B. Li, C. Liang, H. Wang and Z. Qiao, *Appl. Surf. Sci.*, 2016, **362**, 109–114.

69 K. Khlifi, H. Dhiflaoui, A. Ben Rhouma, J. Faure, H. Benhayoune and A. Ben Cheikh Laarbi, *Coatings*, 2021, **11**, 477.

70 R. Drevet, N. B. Jaber, J. Fauré, A. Tara, A. B. Larbi and H. Benhayoune, *Surf. Coat. Technol.*, 2016, **301**, 94–99.

71 K. Cheng, C. Ren, W. Weng, P. Du, G. Shen, G. Han and S. Zhang, *Thin Solid Films*, 2009, **517**, 5361–5364.

72 Y. C. Li, C. Zhang, W. Xing, S. F. Guo and L. Liu, *ACS Appl. Mater. Interfaces*, 2018, **10**, 43144–43155.

73 A. M. Rahimi, M. Cai and S. Hoyer-Fender, *Cells*, 2022, **11**, 2677.

74 A. Turlybekuly, A. D. Pogrebnjak, L. F. Sukhodub, L. B. Sukhodub, A. S. Kistaubayeva, I. S. Savitskaya, D. H. Shokatayeva, O. V. Bondar, Z. K. Shaimardanov, S. V. Plotnikov and B. H. Shaimardanova, *Mater. Sci. Eng., C*, 2019, **104**, 109965.

75 K. M. Nuss and B. von Rechenberg, *Open Orthop. J.*, 2008, **2**, 66.

76 L. Trentani, F. Pelillo, F. C. Pavesi, L. Ceciliani, G. Cetta and A. Forlino, *Biomaterials*, 2002, **23**, 2863–2869.

77 Q. Zhang, J. Dong, M. Peng, Z. Yang, Y. Wan, F. Yao, J. Zhou, C. Ouyang, X. Deng and H. Luo, *Mater. Sci. Eng., C*, 2020, **111**, 110847.

78 S. Saraiva, P. Pereira, C. T. Paula, R. C. Rebelo, J. F. Coelho, A. C. Serra and A. C. Fonseca, *Mater. Sci. Eng., C*, 2021, **131**, 112498.

79 S. Datta, M. Das, V. K. Balla, S. Bodhak and V. K. Murugesan, *Surf. Coat. Technol.*, 2018, **344**, 214–222.

80 P. K. Mattila and P. Lappalainen, *Nat. Rev. Mol. Cell Biol.*, 2008, **9**, 446–454.